© 2021. Published by The Company of Biologists Ltd | Journal of Cell Science (2022) 135, jcs255737. doi:10.1242/jcs.255737

RESEARCH ARTICLE

SPECIAL ISSUE: CELL BIOLOGY OF LIPIDS

Ferroptosis induces membrane blebbing in placental trophoblasts

Kazuhiro Kajiwara[1,2,*], Ofer Beharier[1,*], Choon-Peng Chng[3,*], Julie P. Goff[1], Yingshi Ouyang[1], Claudette M. St Croix[4], Changjin Huang[3,5], Valerian E. Kagan[6], K. Jimmy Hsia[3,5] and Yoel Sadovsky[1,7,‡]

ABSTRACT

Ferroptosis is a regulated, non-apoptotic form of cell death, characterized by hydroxy-peroxidation of discrete phospholipid hydroperoxides, particularly hydroperoxyl (Hp) forms of arachidonoyl- and adrenoyl-phosphatidylethanolamine, with a downstream cascade of oxidative damage to membrane lipids, proteins and DNA, culminating in cell death. We recently showed that human trophoblasts are particularly sensitive to ferroptosis caused by depletion or inhibition of glutathione peroxidase 4 (GPX4) or the lipase PLA2G6. Here, we show that trophoblastic ferroptosis is accompanied by a dramatic change in the trophoblast plasma membrane, with macro-blebbing and vesiculation. Immunofluorescence revealed that ferroptotic cell-derived blebs stained positive for F-actin, but negative for cytoplasmic organelle markers. Transfer of conditioned medium that contained detached macrovesicles or co-culture of wild-type target cells with blebbing cells did not stimulate ferroptosis in target cells. Molecular modeling showed that the presence of Hp-phosphatidylethanolamine in the cell membrane promoted its cell ability to be stretched. Together, our data establish that membrane macro-blebbing is characteristic of trophoblast ferroptosis and can serve as a useful marker of this process. Whether or not these blebs are physiologically functional remains to be established.

KEY WORDS: Ferroptosis, Blebs, Trophoblast, Phospholipids, Simulation

INTRODUCTION

Programmed death plays an essential homeostatic role in vital cellular processes, such as proliferation, differentiation, embryonic development and immunity, by eliminating injured or potentially harmful cells (Fuchs and Steller, 2011; Jacobson et al., 1997). Ferroptosis is a non-apoptotic, iron-dependent form of programmed cell death characterized by excessive accumulation of hydroperoxidized phosphatidylethanolamines (Hp-PEs) particularly those harboring the fatty acyls arachidonoyl (HpETE-PE) and adrenoyl (HpDTE-PE) (Kagan et al., 2017). Ferroptosis is promoted by excess iron and lipoxygenation, glutathione depletion, and deletion or inactivation of the phospholipid peroxidase glutathione peroxidase 4 (GPX4) (Yang et al., 2014; Dixon et al., 2012). Other proteins were recently found to attenuate ferroptotic injury, including the glutathione-independent ferroptosis suppressor protein-1 (FSP1; also known as AIFM2), cytochrome P450 oxidoreductase, transferrin receptor, ferritin, NRF2 (also known as NFE2L2), HMOX1 and prominin 2 (Doll et al., 2019; Gao et al., 2015; Hou et al., 2016; Sun et al., 2016; Kwon et al., 2015; Brown et al., 2019; Zou et al., 2020). Ferroptosis has been implicated in pathological cell death, such as ischemia-reperfusion injury (Eleftheriadis et al., 2018; Linkermann et al., 2014a), neurodegenerative disease (Tuo et al., 2017; Li et al., 2017) and cancer-related cell death (Dixon et al., 2012; Ma et al., 2017; Kinowaki et al., 2018).

Morphological changes that typify diverse forms of programmed cell death are not uniform. Commonly recognized changes include cell rounding, shrinking and, later, plasma membrane rupture as an end-stage event (Dixon et al., 2012; Linkermann et al., 2014b; Galluzzi et al., 2018). Traditionally viewed as a sign of apoptosis (Nelson, 1996), cell death processes include bleb formation, usually mediated by cytoskeletal restructuring. Bleb formation can be initiated by a local detachment of the actin cortical cytoskeleton from the membrane, with a spherical protrusion, followed by plasma membrane rupture (Cunningham, 1995; Charras and Paluch, 2008; Coleman et al., 2001). Blebbing is a dynamic process that depends on cellular reorganization associated with cytokinesis (Charras and Paluch, 2008), cell spreading (Norman et al., 2010), virus uptake (Mercer and Helenius, 2008; Gruenberg and van der Goot, 2006), apoptosis (Coleman et al., 2001), and locomotion of tumor and embryonic cells (Fedier and Keller, 1997; Shi et al., 2005). However, there are scant data on the biology of blebbing during ferroptosis (Belavgeni et al., 2019). This is particularly germane in light of the potential role of blebbing in cell signaling or tumor cell invasion (Voura et al., 1998) or physiological migration during development.

A few recent studies implicate placental ferroptosis in pregnancy complications (Beharier et al., 2020; Zhang et al., 2020; Ng et al., 2019), adding a broader dimension to our understanding of the placental lipotoxic injury that underlies common diseases during human pregnancy. In addition to the sensitivity of human placental trophoblasts to ferroptosis induced by pharmacologic or genomic inhibition of GPX4, we recently identified a novel role for the lipase PLA2G6 in placental ferroptosis (Beharier et al., 2020). During our investigation, we noticed the formation of large blebs (‘macro-blebbing’) in trophoblasts undergoing ferroptosis. Here, we examine bleb formation by ferroptotic trophoblasts, analyze the bleb content and the potential effect of blebbing on neighboring cells, carry out molecular simulation on effects of hydroperoxidation on membrane biophysical properties, and investigate components that might contribute to enhanced blebbing in human placental trophoblasts.

[1]Magee-Womens Research Institute, Department of Obstetrics, Gynecology and Reproductive Sciences, University of Pittsburgh, Pittsburgh, PA 15213, USA. [2]Department of Obstetrics and Gynecology, Jikei University School of Medicine, Tokyo, Japan 105-8461. [3]School of Mechanical and Aerospace Engineering, Nanyang Technological University, Singapore 639798, Republic of Singapore. [4]Department of Cell Biology, University of Pittsburgh, Pittsburgh, PA 15261, USA. [5]School of Chemical and Biomedical Engineering, Nanyang Technological University, Singapore 637459, Republic of Singapore. [6]Department of Environmental and Occupational Health, University of Pittsburgh, Pittsburgh, PA 15261, USA. [7]Department of Microbiology and Molecular Genetics, University of Pittsburgh, Pittsburgh, PA 15213, USA.
*These authors contributed equally to this work

‡Author for correspondence (ysadovsky@mwri.magee.edu)

K.K., 0000-0003-4358-8791; O.B., 0000-0001-5317-4512; C.-P.C., 0000-0002-3707-8747; Y.O., 0000-0002-8970-1297; C.M.S.C., 0000-0003-0794-4939; V.E.K., 0000-0002-7245-1885; Y.S., 0000-0003-2969-6737

Handling Editor: David Stephens
Received 14 October 2020; Accepted 15 December 2020

Journal of Cell Science (2022) 135, jcs255737. doi:10.1242/jcs.255737

RESULTS

Trophoblast ferroptosis is accompanied by macro-blebbing

The characteristic morphology of ferroptotic cells includes a normally sized nucleus that lacks chromatin condensation, but with shrunken, dense mitochondria (Wang et al., 2020; Dixon et al., 2012; Xie et al., 2016; Doll and Conrad, 2017). In our analysis of ferroptosis in either primary human trophoblasts (PHT cells) or the BeWo human trophoblast cell line exposed to the GPX4 inhibitor RSL3, we detected the frequent appearance of large blebs ('macro-blebs', Fig. 1A; Movie 1), measuring 10–53 µm in diameter. We observed similar macro-blebbing in two additional BeWo models that predispose cells to ferroptosis, CRISPR-Cas9-mediated knockout (KO) of *PLA2G6* or shRNA-mediated silencing of *GPX4* (*shGPX4*) (Fig. 1A,B). Notably, the blebs appeared independently of cell shrinkage (Movie 1). We validated the time-course and concentration dependence of the ferroptotic process in BeWo cells by measuring lactate dehydrogenase (LDH) release, a commonly used assay for cell death, and which can be inhibited by the ferroptosis inhibitor ferrostatin-1 (Fer-1, Fig. 1B,C) (Dixon et al., 2012). As expected, we found an increase in cell death and macro-blebbing in BeWo cells deficient in PLA2G6 (Fig. 1C–E). We also used inverted microscopy alongside live-cell imaging using

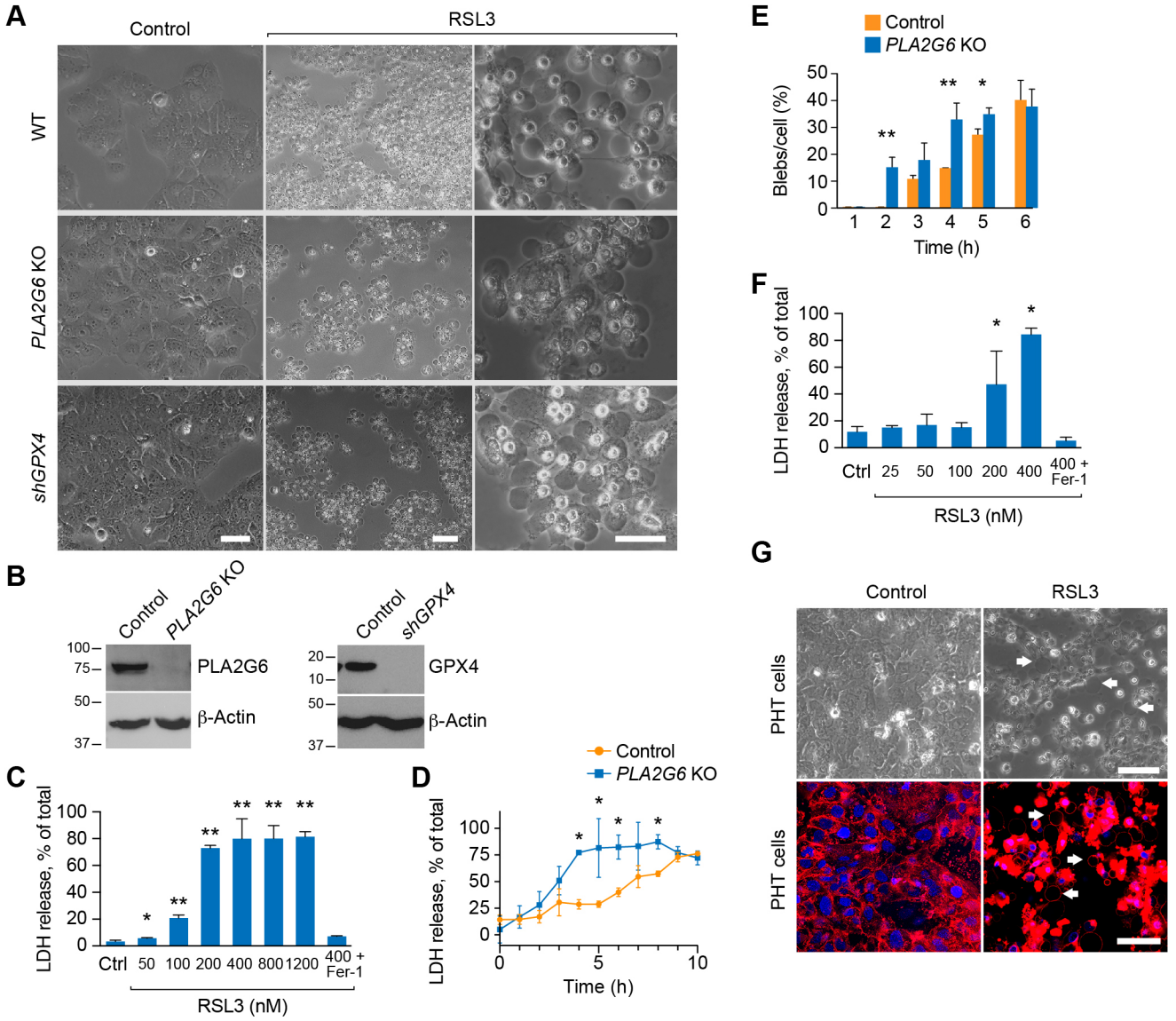

Fig. 1. Ferroptosis causes macro-blebbing in trophoblasts. (A) Phase-contrast microscopy images of macro-blebs in WT BeWo (upper panels), *PLA2G6* KO (middle panels) and *shGPX4* (lower panels). The cells were exposed to vehicle control (left panels) or RSL3 (100 nM, middle, low magnification and right, high magnification) for 8 h for WT cells or for 4–5 h for *PLA2G6* KO or *shGPX4* cells. Scale bars: 50 µm. (B) Western immunoblotting of PLA2G6 an GPX4 in *PLA2G6* KO and *shGPX* cells. (C) Ferroptotic BeWo cell death, induced by increased RSL3 concentrations and assessed after 24 h by the LDH release assay as described in the Materials and Methods. Cell death was inhibited by ferrostatin-1 (Fer-1, 0.5 µM). Values are mean±s.d. **P*<0.05, ***P*<0.01 compared to control (one-way-ANOVA with Tukey's method for multiple comparisons). (D) A time-course of the effect of RSL3 (100 nM) on ferroptosis, assessed by the LDH release assay in WT versus *PLA2G6* KO BeWo cells. Values are mean±s.d. **P*<0.05 (unpaired two-tailed *t*-test). (E) Bleb formation in WT vs *PLA2G6* KO BeWo cells, exposed to RSL3 (100 nM). Values are the number of counted blebs per total cells in the field (%), as detailed in Materials and Methods, shown as means±s.d. **P*<0.05, ***P*<0.01 (unpaired two-tailed *t*-test). (F) The same concentration-dependence experiment as in C, performed using PHT cells. (G) Macro-blebbing in PHT cells exposed to RSL3 (100 nM) versus vehicle control, assessed using phase-contrast microscopy images (upper panels) or CellMask stains (lower panel). White arrows indicate representative blebs. Scale bars: 50 µm. All panels represent three independent experiments.

Journal of Cell Science

Journal of Cell Science (2022) 135, jcs255737. doi:10.1242/jcs.255737

CellMask, an amphipathic, lipophilic membrane dye, to confirm RSL3-induced blebbing in PHT cells (Fig. 1F,G). The enhanced CellMask signal in RSL3-exposed cells, also seen in Figs 3 and 5G, likely represents cell shrinkage and membrane collapse (as observed in Movie 1). We noted that >4 h of RSL3-induced ferroptosis was no longer reversible with Fer-1 (Fig. S1A).

We compared the sensitivity to ferroptosis-induced bleb formation in trophoblasts to diverse cell types exposed to RSL3. Because it has been shown that susceptibility to ferroptosis depends on cell density (Yang et al., 2019; Wu et al., 2019), we assessed cell viability and bleb formation at low (<50%) and high (>80%) cell density. Notably, density affected mainly BeWo trophoblast cells (Fig. S1B), with minimal effect on other cell types. We found the greatest LDH release and blebbing in the trophoblastic BeWo and PHT cells, as well as in the MDA-MB-231 breast cancer line and human umbilical vein endothelial cells (HUVECs), with resistance to ferroptosis and blebbing in HeLa, Caco-2, U2OS lines and primary placental fibroblasts (PPF cells) (Fig. 2A,B; Fig. S1B–I). Induction of apoptosis (by staurosporine; Aoki et al., 2020; Sebbagh et al., 2001) in BeWo or PHT cells exhibited minimal blebbing (Fig. 2C,D).

Cellular cargo in ferroptotic macro-blebs

To determine whether ferroptotic blebs harbor cellular organelles, we used live imaging of BeWo cells, stained for mitochondria (MitoTracker), lysosomes (LysoTracker), DNA (DAPI) lipid droplets (BODIPY 493/503), and mNeonGreen tagged with the endoplasmic reticulum retention signal KDEL (Semenza et al., 1990). The cells were co-stained with the plasma membrane stain CellMask, as control. As shown in Fig. 3, ferroptosis-stimulated blebs were positive for CellMask (Figs 1G and 3), but negative for the other cell structures. We confirmed the presence of F-actin in blebs using live cell imaging of mRNA LifeAct-TagGFP2 (Fig. 3, bottom right). We next sought to assess whether macro-blebs can be detached from cells as free macro-vesicles yet noted that, upon paraformaldehyde-based cell fixation for antibody staining, the macro-blebs were not stable and might have also been washed away. Using iPGell fixative (see Materials and Methods), we were able to detect blebs that were detached as macrovesicles positive for CellMask but negative for tubulin (Fig. S2A,B). To assess whether myosin II was functionally involved in bleb formation, we tested the effect of blebbistatin, a myosin II inhibitor, on blebbing (Taneja et al., 2020). Exposure to blebbistatin had no effect on LDH release or bleb formation (Fig. S2C–E), indicating that myosin II was not involved in the formation of ferroptotic macro-blebs.

The effect of ferroptotic BeWo blebs on neighboring cells

It has been reported that the ferroptotic signal might be transmitted within tissues in a wave-like manner (Linkermann et al., 2014a). To investigate whether released blebs led to transmission of the ferroptotic signal, we silenced *GPX4* expression in BeWo cells (Fig. 4A) and tested for the effect of conditioned medium (CM) from the ferroptotic cells on target wild-type (WT) BeWo cells exposed to a low level of RSL3. We found no evidence for enhancement of ferroptosis by incubation of WT BeWo cells with CM from *shGPX4* ferroptotic cells (Fig. 4A). Similarly, isolated small extracellular vesicles (sEVs), microvesicles (MVs) or apoptotic blebs (ABs) from the CM of ferroptotic cells had no effect on ferroptosis in target cells (Fig. 4B). We also showed that the degree of ferroptosis in a mixture of ferroptotic cells (generated by silencing *GPX4*) was directly proportional to the fraction of *shGPX4* cells, suggesting that the ferroptotic signal did not propagate to WT cells (Fig. 4C). To obtain additional support for these observations, we co-cultured green fluorescent protein (GFP)-labeled *shGPX4* BeWo cells with red fluorescent protein (RFP)-labeled WT BeWo cells (Fig. 4D, upper panel). Upon addition of RSL3 to induce ferroptosis (Fig. 4D,

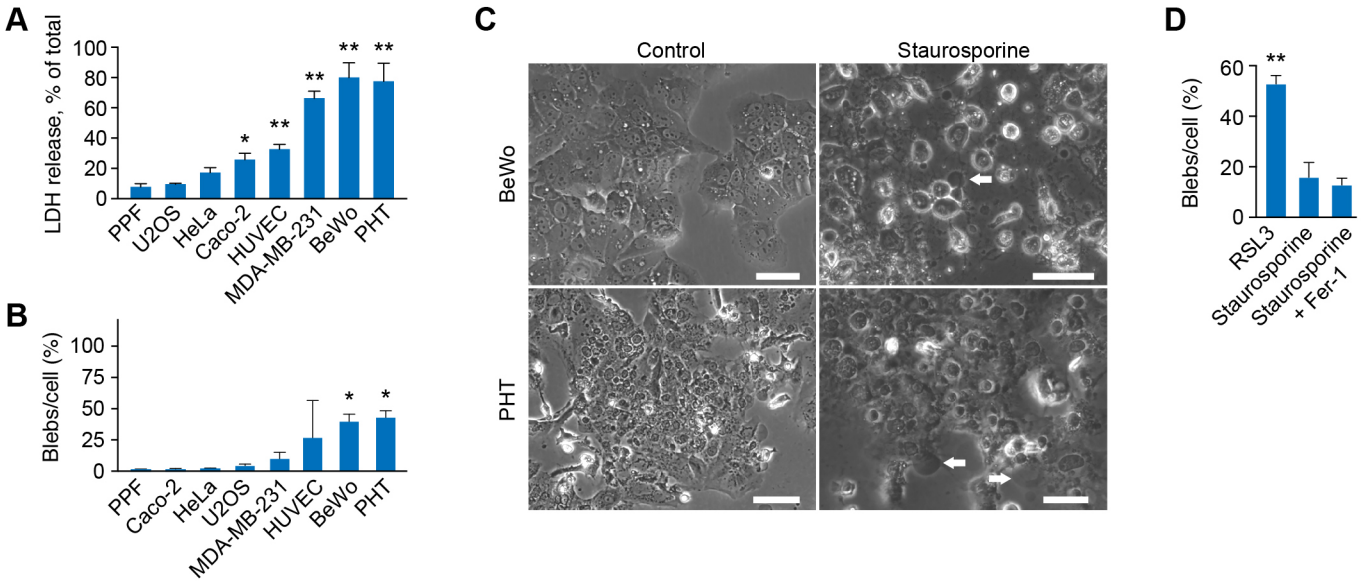

Fig. 2. Ferroptosis and bleb formation in various cell types. (A) The effect of RSL3 (800 nM, 24 h) on ferroptosis in several cell types, as detailed in the text. Ferroptosis was measured by the LDH release assay, as described in Materials and Methods. Values are mean±s.d. **P*<0.05, ***P*<0.01 compared to PPF cells (one-way-ANOVA with Tukey's method for multiple comparisons). (B) Bleb formation in several cell types (as in A), exposed to RSL3 (800 nM, 24 h). Values are the number of counted blebs per total cells in the field (%), as detailed in Materials and Methods, shown as means±s.d. **P*<0.05 compared to PPF cells (one-way-ANOVA with Tukey's method for multiple comparisons). (C) Phase contrast microscopy of bleb formation in BeWo (upper panels) or PHT cells (lower panels), exposed to vehicle control versus staurosporine (1 µM for 6 h). White arrows indicate representative blebs. Scale bars: 50 µm. (D) Bleb formation in BeWo cells, assessed as described in B, comparing the effect of RSL3 and 1 µM of staurosporine (6 h), in the absence or presence of the ferroptosis inhibitor Fer-1 (0.5 µM). Values are mean±s.d. ***P*<0.01 compared to RSL3 (one-way-ANOVA with Tukey's method for multiple comparisons). All panels are representative of three independent experiments.

Journal of Cell Science (2022) 135, jcs255737. doi:10.1242/jcs.255737

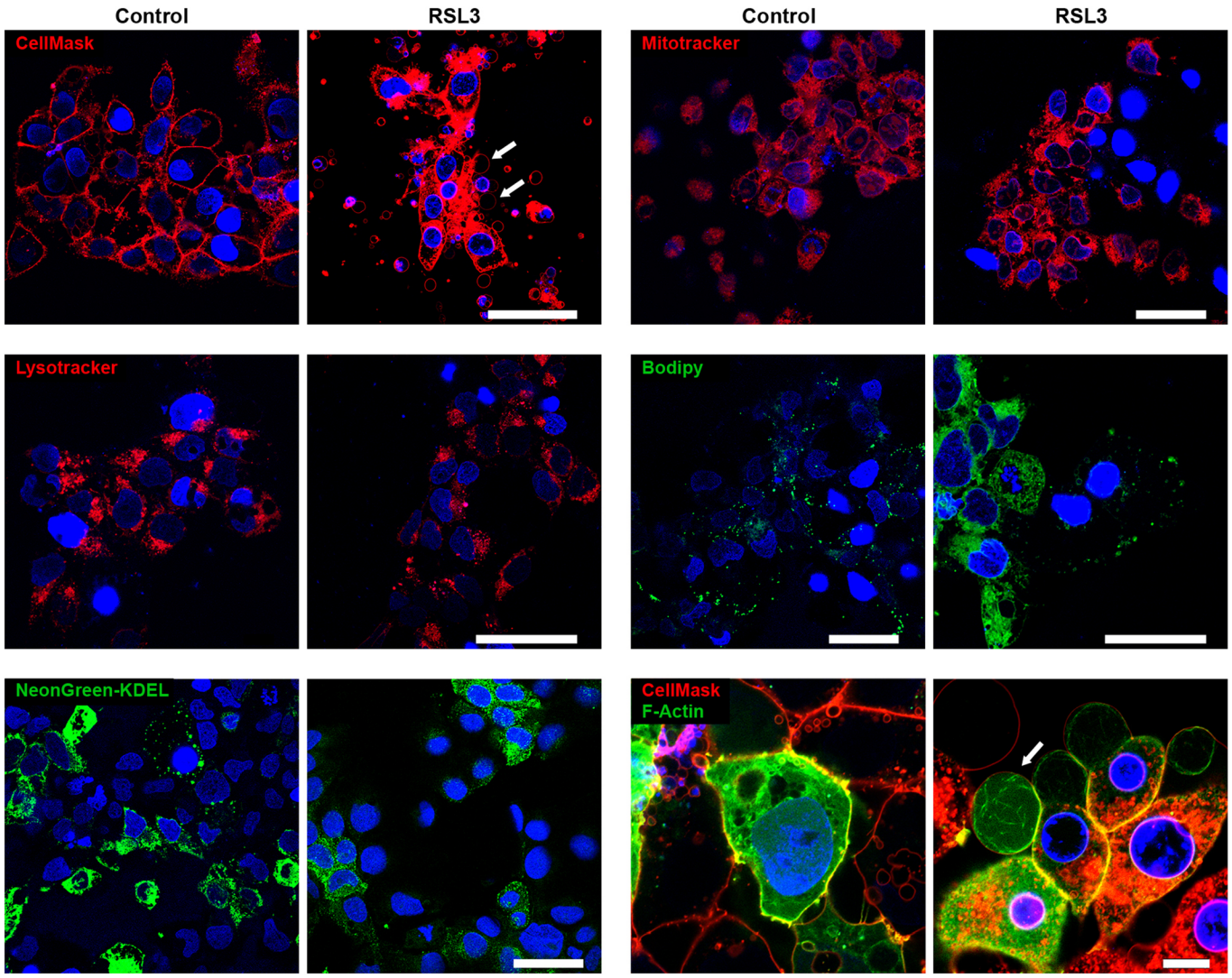

Fig. 3. Analysis of subcellular components in BeWo macro-bleb cargo. Panels show live-cell images of BeWo cells processed for imaging with CellMask (cell membrane, red), MitoTracker (mitochondria, red), LysoTracker (lysosomes, red), Bodipy 493/503 (lipids, green), mNeonGreen tagged with the endoplasmic reticulum retention signal KDEL (green) or F-actin (actin, green). The cells were exposed to vehicle control or RSL3 (200 nM, 8 h) after the cells were stained with each probe as detailed in Materials and Methods. Nuclei were stained with DAPI. White arrows in some of the panels point to macro-blebs. The images shown are representative of three independent experiments. Scale bars: 50 µm.

middle and lower panels), we found that blebbing was restricted to the *shGPX4*- plus GFP-expressing (*shGPX4*-GFP) cells, with no evidence for the spread of blebbing to the RFP-expressing target cells. Notably, a low level of blebbing was seen in WT target cells after 24 h (Fig. 4D, lower panels), likely reflecting the effect of RSL in the medium, as it was also observed using a co-culture of GPX4-GFP-expressing cells and RFP-expressing cells (Fig. 4D, middle). We confirmed these results using a similar strategy in which BeWo cell ferroptosis was induced by *PLA2G6*-KO RFP-expressing cells and GFP-expressing WT BeWo cells. Again, blebbing was restricted to the ferroptotic cells, with no evidence for ferroptotic signal propagation to WT target cells (Fig. 4E). Together, these data suggest that ferroptosis-related blebs, extracellular vesicles (EVs) or CM are unlikely to transmit a ferroptotic signal to neighboring cells.

The role of syncytin in ferroptotic bleb formation

The process of cytotrophoblast fusion into syncytiotrophoblasts is mediated by the fusogenic proteins syncytin-1 and 2 (also known as ERVW1 and ERVFRD1, respectively), which are expressed primarily in placental trophoblasts (Mi et al., 2000; Hernández and Podbilewicz, 2017; Lavialle et al., 2013; Gerbaud and Pidoux, 2015). As part of the fusion process, these proteins bend and destabilize the lipid bilayer of the cell membrane (Gerbaud and Pidoux, 2015). On the basis of these data, we asked whether syncytins might promote macro-blebbing during trophoblast ferroptosis. As expected, the expression of syncytin-1 and -2 was highest in PHT cells and in the BeWo trophoblast line compared to other cell types (Fig. 5A,B). In addition, exposure of BeWo cells to forskolin heightened their ferroptosis sensitivity (Fig. 5C). However, we found that RSL3 stimulation did not induce syncytin expression (Fig. S3B). Moreover, knockdown (KD) of syncytin-1, -2 or both (Fig. S3D–F) had no effect on RSL3-induced ferroptosis (Fig. 5D–F) and bleb (Fig. 5G,H). Taken together, syncytin-1 or -2 is not a key factor that determines macro-blebbing in ferroptotic trophoblasts.

Simulation of PE hydroperoxidation effect on membrane properties

We sought to perform systematic coarse-grained molecular dynamics-based simulation of membrane phospholipids in order to

Journal of Cell Science (2022) 135, jcs255737. doi:10.1242/jcs.255737

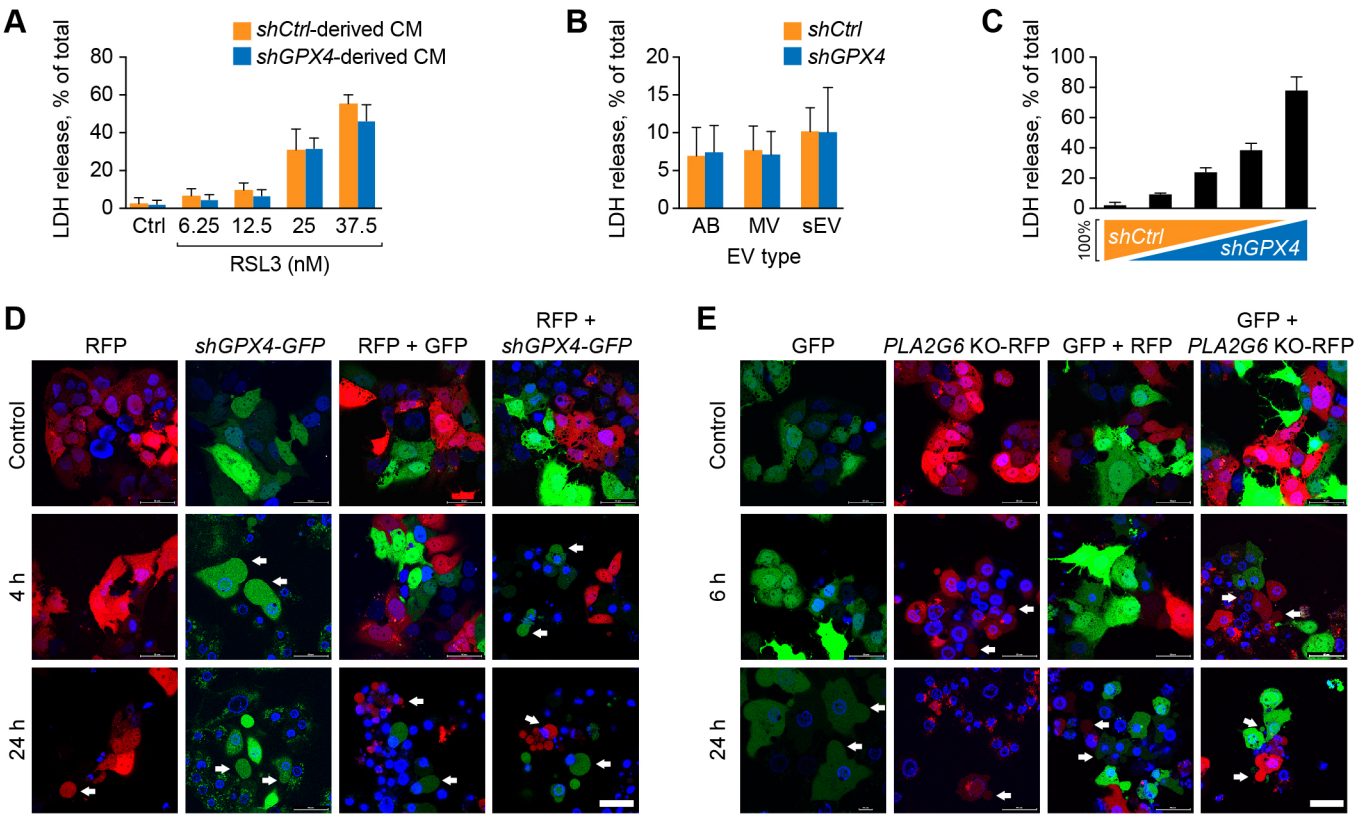

Fig. 4. Ferroptotic cells do not transfer a ferroptotic signal to neighboring WT cells. (A) The effect of conditioned medium (CM), derived from WT or sh*GPX4* BeWo cells, on ferroptosis in recipient WT BeWo cells. The CM was harvested followed by centrifugation of CM at 500 ***g*** for 10 min to remove cell debris. The recipient cells were exposed to CM for 8 h and then washed and cultured in serum-free medium with a range of concentrations of RSL3 for 24 h. Ferroptosis was measured by the LDH release assay as described in Materials and Methods. Values are shown as means±s.d. Data were analyzed by unpaired two-tailed *t*-test (no significant differences were found between control shRNA and *shGPX4*). (B) The effect of isolated extracellular vesicles (EVs) from *shGPX4* BeWo cells versus WT BeWo cells, both exposed to RSL3 (25 nM, 24 h). Ferroptosis was determined after 24 h of incubation with EVs, using the LDH release assay, as described in the Materials and Methods. AB, apoptotic bodies; MV, microvesicles; sEV, small extracellular vesicles. The EVs were isolated as detailed in Materials and Methods. Values are shown as means±s.d. Data were analyzed using unpaired two-tailed *t*-test (no significant differences were found between control shRNA and *shGPX4*). (C) Co-cultures of WT and *shGPX4* BeWo cells, exposed to RSL3, 25 nM for 24 h. The percentage of WT and *shGPX4* types was 100/0, 75/25, 50/50, 25/75, and 0/100, respectively. Ferroptosis was determined by the LDH release assay, as described in Materials and Methods. (D,E) The effect of co-culturing ferroptotic *shGPX4* BeWo with WT BeWo cells (D) or ferroptotic *PLA2G6* KO with WT BeWo cells (E) on bleb formation in WT BeWo cells. The cells were cultured on glass bottom dishes. In D, ferroptotic cells were transfected with GFP and WT cells with RFP. In panel E, ferroptotic cells were transfected with RFP and WT cells with GFP, as described in the Materials and Methods. All cells were co-stained with DAPI. The upper panels show cultures without added RSL3 and the lower panels show cultures with added 25 nM RSL3 for 4 h or 24 h. Note that, at 24 h with RSL3, even some of the control cells started exhibiting blebbing, as shown in both D and E. White arrows indicate representative blebs. Scale bars: 50 µm. All panels and images are representative of three independent experiments.

assess the effect of hydroperoxidation on membrane biophysical properties. For this purpose, we compared the effect of peroxidation on 1-stearoyl-2-arachidonoyl-glycero-3-phosphorylcholine (SAPC) or 1-stearoyl-2-arachidonoyl-glycero-3-phosphorylethanoamine (SAPE). This was undertaken by attaching a coarse-grained polar particle representing the hydroperoxide functional group (-OOH) to either the C12 or C15 site of the unsaturated fatty acid tail (Fig. 6A). The simulations show that peroxidation at the C12 and C15 sites made the lipid bilayer more flexible (Fig. 6B). Close inspections of the orientation of SAPE and SAPC lipids in the bilayer revealed that the hydroperoxidated unsaturated fatty acid tail tended to tilt in such a way that the OOH particles became closer to the phospholipid head-group region (Fig. 6C). The tilting of the unsaturated tails led to reduction of the order parameter (see Materials and Methods), averaged over all the C–C bonds along the two fatty acid tails (Fig. 6D), suggesting that peroxidation was associated with more disorganized membrane lipid packing, which would exhibit greater flexibility over the course of the simulation (Fig. 6B). Notably, peroxidation at C15 resulted in a lower averaged order parameter than peroxidation at C12 for both SAPE and SAPC bilayers.

We further assessed the membrane biophysical properties as a function of lipid hydroperoxidation. As shown in Fig. 7A, simulation results show that the area occupied by each lipid molecule (i.e. area/lipid) increases linearly with increasing peroxidation, consistent with the change in average order parameter (Fig. 6D). Furthermore, peroxidation at C15 leads to a greater effect than that at C12, indicating that the deeper C15 position inside the bilayer hydrophobic interior renders a greater tilt of the fatty acid tail than that at C12. The greater tilt of C15 fatty acid tails in phosphorylcholine (PC) or PE bilayers also results in a thinner bilayer than that with C12 peroxidation (Fig. 7B). The area/lipid of PE bilayers was smaller than that of PC bilayers (Fig. 7A) as the PE head groups are more attracted to each other due to their capability to form hydrogen bonds.

On the basis of these data, we simulated membrane stretching and evaluated the fractional increase in membrane area with the

Journal of Cell Science (2022) 135, jcs255737. doi:10.1242/jcs.255737

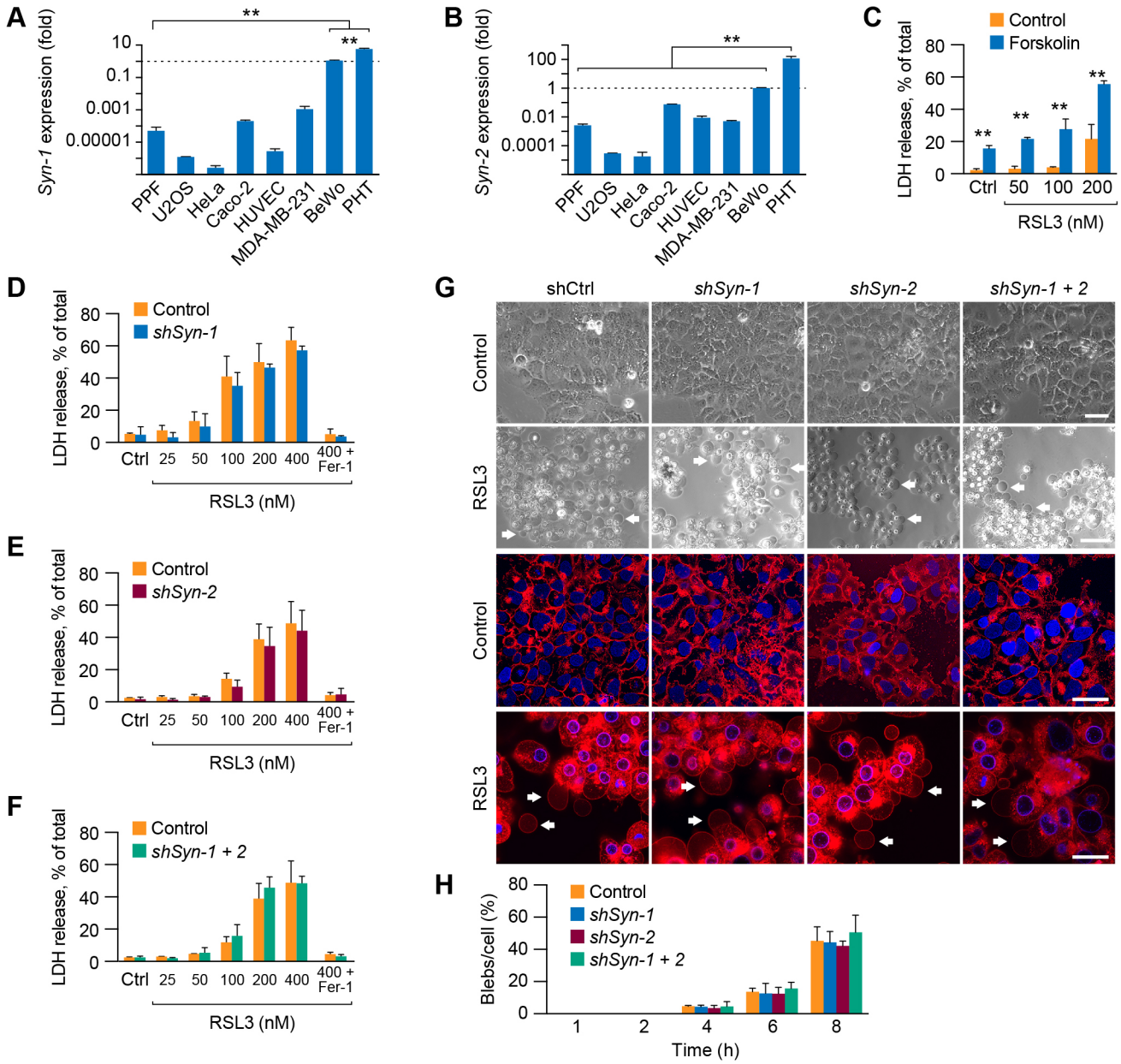

Fig. 5. Syncytin-1 and -2 do not play a role in ferroptosis in BeWo cells. (A,B) The expression of syncytin-1 (Syn-1) and syncytin-2 (Syn-2) in various cell types used in our study. Expression was determined using RT-qPCR as detailed in Materials and Methods, and all relative expression values were compared to RNA expression in BeWo cells, defined as 1. Values are shown as mean±s.d. $^{**}P<0.01$ (one-way-ANOVA with Tukey's method for multiple comparisons). (C) The effect of forskolin (60 µM for 48 h, and RSL at various concentrations), which stimulates BeWo cell fusion, on ferroptosis, measured by LDH release assay as described in Materials and Methods. Values are shown as mean±s.d. $^{**}P<0.01$ (unpaired two-tailed *t*-test). (D–F) The effect of knockdown of *Syn-1* (D), *Syn-2* (E) or both *Syn-1* and *Syn-2* (F) on cell susceptibility to RSL3-induced (8 h) ferroptosis. Silencing of *Syn-1* and *-2* and assessment of ferroptosis, measured using the LDH release assay, were performed as detailed in Materials and Methods. Fer-1 was used to block ferroptosis, as a control. Values are shown as mean ±s.d. Data were analyzed using unpaired two-tailed *t*-test (no significant differences were found between control shRNA *shSyn-1, shSyn-2* or both *shSyn1+2*). (G) The effect of KD of *Syn-1*, *Syn-2* or both on BeWo blebbing, in the absence or presence of RSL3 (200 nM for 8 h). CellMask was added in the lower panels to enhanced visualization of blebs, also highlighted using white arrows. Scale bars: 50 µm. (H) Bleb formation in BeWo cells, based on the paradigms shown in G. Values are the number of counted blebs per total cells in the field (%), as detailed in Materials and Methods, shown as means±s.d., compared to control. Data were analyzed by one-way-ANOVA with Tukey's method for multiple comparisons test (no significant differences were found between control shRNA and *shSyn-1, shSyn-2* or both *shSyn1+2*). The data represent three independent experiments for A-C,G,H and six independent experiments for D-F.

membrane tension. This enabled us to estimate the membrane elastic modulus K_A (a measure of the resistance to stretching, Fig. S4). Fig. 7C shows that K_A monotonically decreases with increasing fraction of oxidized lipids for both SAPE and SAPC. For the native membranes, SAPE shows a larger K_A value than SAPC, consistent with the more tightly packed, thicker PE membrane, as we have previously observed (Peng et al., 2021). As the fraction of oxidized lipids increases beyond 25%, simulation results show that the resistance to stretching of the SAPE bilayer becomes lower than that of SAPC bilayer, allowing for greater membrane stretching. Decreases in the membrane elastic modulus allow the membrane to stretch more easily, thus enabling bleb formation under a given

Journal of Cell Science (2022) 135, jcs255737. doi:10.1242/jcs.255737

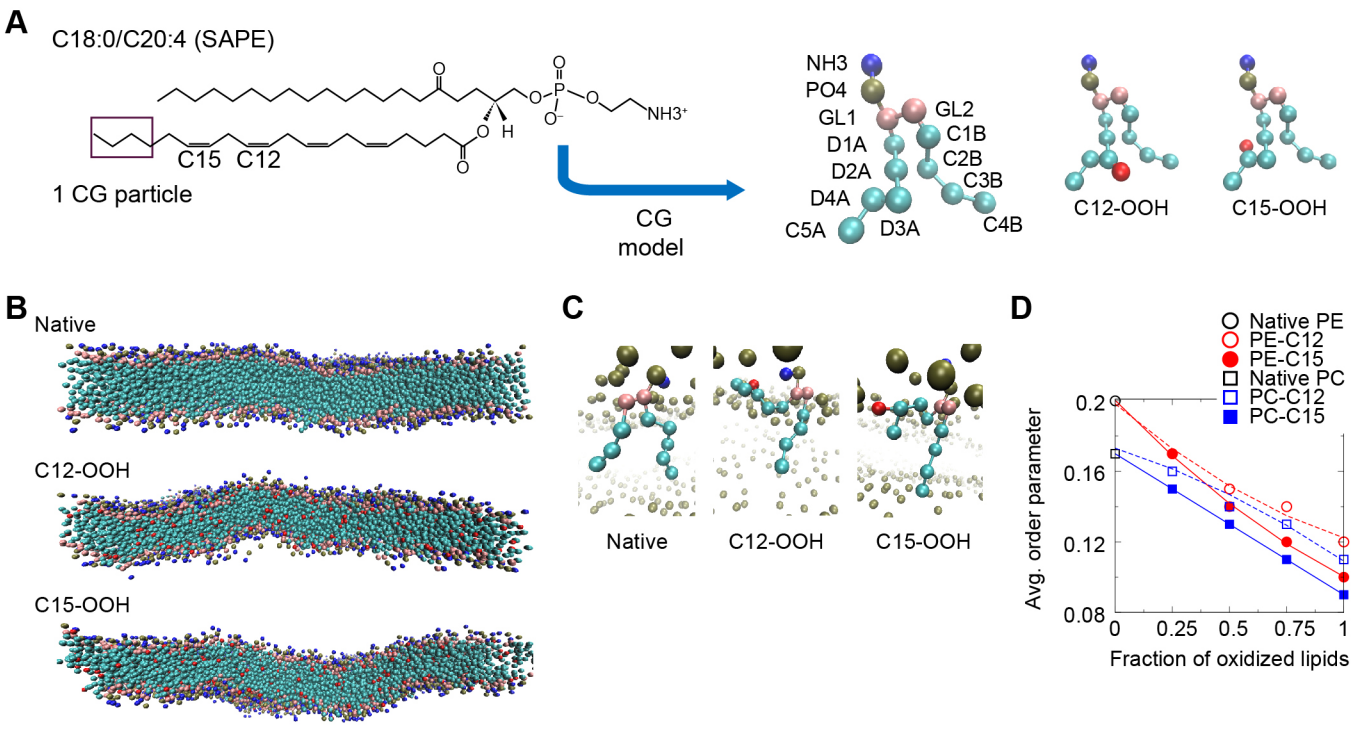

Fig. 6. Coarse-grained molecular dynamics simulations of SAPE and SAPC lipid membranes. (A) Left panel, the chemical structure of SAPE lipid molecule with locations of the four C–C double-bonds indicated. SAPC is similar but with the NH_3 group substituted by the NC_3 group. Middle and right panels, coarse-grained (CG) models (4 atoms to 1 particle mapping) of unoxidized (native) SAPE lipid, oxidized SAPE with hydroperoxide functional group (-OOH) linked to a D3A particle that includes C12 (C12-OOH) and to a D4A particle that includes C15 (C15-OOH). Head-group NH3 particle in blue; PO_4 particle in dark green; glycerol particles (GL1 and GL2) in pink, carbon particles in cyan ('D' particles contain double-bonds whereas 'C' particles contains only single-bonds); and OOH particle in red. (B) Equilibrated configurations of native SAPE, C12-OOH and C15-OOH bilayers after 2 µs simulation (solvent omitted for clarity). (C) Orientation of representative native and oxidized SAPE lipids in the bilayer at the end of each 2-µs simulation. (D) Mean values of order parameter computed on the basis of the angle between each tail bond and the bilayer normal, with averaging done over all the C–C bonds. The error bars were omitted as the standard errors are of the order of 0.001, or <1% of the averaged values.

intracellular pressure. This mechanism might play an important role in the observed macro-blebbing during ferroptosis.

DISCUSSION

We showed that trophoblasts are sensitive to ferroptosis and that this form of cell death promotes blebbing in either primary trophoblasts or the BeWo trophoblast line. Our live-cell images reveal that blebs commonly reached the size of the entire cell. Hence, we termed the process macro-blebbing to distinguish these blebs from the smaller blebs that may accompany other forms of cell death (Aoki et al., 2020; Tinevez et al., 2009; Belavgeni et al., 2019; Nganga et al., 2019). Interestingly, bleb formation has been described as a protective mechanism, designed to reduce the intracellular hydrostatic pressure during osmotic malfunction (Ruan et al., 2015). Our video-imaging shows that ferroptotic macro-blebbing might appear either before or after cell contraction or disintegration, suggesting that this process is a passive one, driven by osmotic pressure, which characterizes inactivation of membrane osmotic pumps during cell death.

We were able to examine the content of attached blebs, and even detached vesicles, using a combination of live-cell dyes and also iPGell technology, which enabled gentle, rapid fixation that preserved bleb morphology. Using these techniques, we found

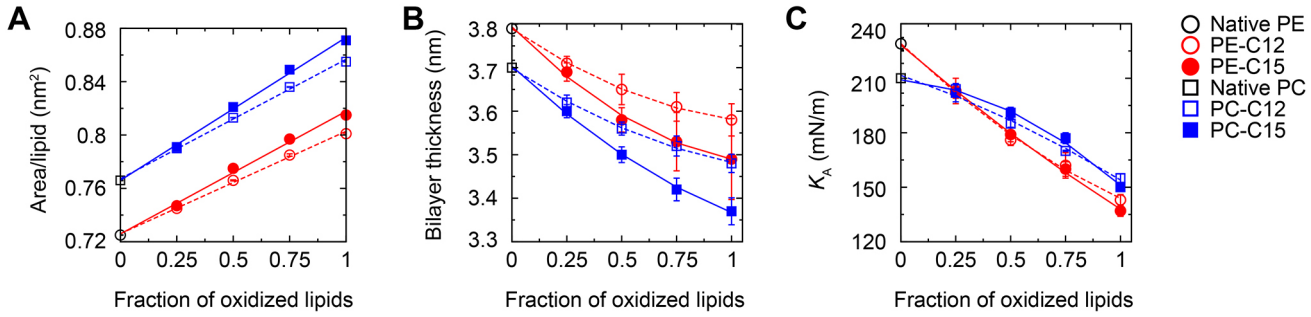

Fig. 7. The effect of increasing the fraction of oxidized lipids in SAPE and SAPC bilayer membranes on the physical and mechanical membrane properties. The effect of increasing the fraction of oxidized lipids in SAPE and SAPC bilayer membranes was revealed by coarse-grained molecular dynamics simulations. (A) Area per lipid, computed by dividing the simulation box area by the number of lipids in the system. (B) Bilayer thickness computed on the basis of location of head-group particles between the two monolayers. (C) The elastic moduli estimated by simulated membrane stretching.

Journal of Cell Science (2022) 135, jcs255737. doi:10.1242/jcs.255737

that attached and detached trophoblastic macro-blebs contain F-actin but not other organelles. Actin, alongside ezrin, actin-bundling and contractile proteins, has been previously reported as being recruited to non-ferroptotic blebs (Charras et al., 2006), and might assist in bleb enlargement. In addition, the serine/threonine kinase ROCK1 also plays a role in bleb formation (Maeda et al., 2016; Claassen et al., 2009), with blebbing dependent on the supply of Ca^{2+} (Jansen et al., 2019), suggesting that discrete signaling events regulate bleb formation. Whether or not these signals are relevant to ferroptotic macro-blebbing remains to be established.

In experiments with transfer of conditioned medium or the co-culture of fluorescently labeled ferroptotic and non-ferroptotic cells, we could not detect any evidence for the transfer of the ferroptotic signal from one cell population to another. Others have shown that sEVs can transfer a pro-apoptotic signal to other cell types (Shen et al., 2020; Ke et al., 2020). In the context of ferroptosis, ferritin-containing sEVs were shown to transport iron out of the cell, thus attenuating ferroptosis (Brown et al., 2019). Dai et al. recently reported that autophagy-dependent ferroptosis is associated with the release sEVs that contain $KRAS^{G12D}$, resulting in fatty acid oxidation in target macrophages (Dai et al., 2020). When isolating several types of EV from ferroptotic BeWo cells and applying them to WT target cells, we found no evidence for stimulation of ferroptosis in non-ferroptotic cells, suggesting that any effect of ferroptosis-related EVs on neighboring cells might be cell type or context specific. Notably, while we were able to visualize released macro-blebs in the cell culture medium using iPGell, we could not isolate intact blebs due to their fragility. Future biochemical analysis of macro-bleb content may point to signals that serve in cell–cell communication.

Searching for membrane proteins that might predispose to ferroptosis, we found that the trophoblast-enriched, fusogenic proteins syncytin-1 or -2 did not contribute to trophoblast blebbing. Importantly, our simulation studies indicate that the conformational change of SAPE and SAPC lipids due to hydroperoxidation has a significant impact on the biophysical properties of the lipid bilayers, with reduced thickness and increased area/lipid upon lipid peroxidation. Similar changes have been reported in studies on other types of phospholipid bilayers (Guo et al., 2016; Weber et al., 2014; Agmon et al., 2018; Rosa et al., 2018). Notably, SAPE peroxidation at the C15 site, which commonly occurs during the process of ferroptosis (Anthonymuthu et al., 2018), may have the greatest effect on the membrane elastic modulus. In the extreme case of full oxidation, the elastic modulus decreases by more than 40%. When the native and fully peroxidized SAPE membranes were subjected to osmotic pressure, lipid membrane tension developed according to Laplace's law. Compared to the native SAPE lipid membrane, the fractional areal strain of the fully oxidized membrane is expected to be 67% higher than that of non-oxidized membrane. Thus, the enhanced ability to be stretched of peroxidized membranes may contribute to ferroptosis-induced membrane macro-blebbing. It should be noted that the fraction of hydroperoxidized PE among membrane phospholipids in ferroptotic cells is likely much lower than the fraction assumed in our modeling, yet hydroperoxidized PE may be decomposed to secondary oxidatively truncated species, resulting in higher amount of hydroperoxidized species.

The membrane macro-blebbing process results in a sudden increase of bleb size (Movie 1), indicative of an instability. The underlying mechanisms of such instability may be mechanical in nature, where membrane peroxidation is not uniform throughout the cell surface. When a patch of membrane undergoes peroxidation, it becomes less stiff, that is, its elastic modulus decreases, inducing a sudden increase in stretching, similar to the sudden inflation of a tubular balloon under increasing internal pressure (Mao et al., 2014). Alternatively, the mechanism may reflect the dynamic process of lipid peroxidation. Localized lipid peroxidation may facilitate peroxidation of surrounding lipids, thus inducing a positive feedback which leads to instability. Assessing these possibilities will require future experiments and models.

We showed that primary trophoblasts and trophoblast cell lines are more susceptible to RSL3-induced ferroptosis than several other commonly used cell lines. Consistent with this observation, it is known that iron, which is needed for ferroptosis-related lipid peroxidation is abundant in trophoblasts (Ng et al., 2019; Fisher and Nemeth, 2017). In addition, reduced or mutated GPX4 has been associated with human placental dysfunction and preeclampsia, and ferroptosis inhibitors attenuate preeclampsia-like symptoms in rats (Peng et al., 2016; Mistry et al., 2010; Zhang et al., 2020). Physiologically, the placenta is exposed to hypoxia and re-oxygenation during normal development, when blood supply to the intervillous space is established and the placenta transitions from histotrophic to hemotrophic support at the end of the first trimester of human pregnancy (Soares et al., 2017; Burton et al., 2002). The placenta is also normally exposed to cycles of reduced and restored blood flow during uterine contractions before and during labor (Alotaibi et al., 2015; Brar et al., 1988), similar to the hypoxia-reperfusion associated with ferroptosis in the brain, kidneys and other organs (Friedmann Angeli et al., 2014; Schoots et al., 2018; Wenzel et al., 2017). This type of injury has been implicated in the placental dysfunction underlying fetal growth restriction, preeclampsia and related conditions (Burton and Jauniaux, 2018; Hung et al., 2002; Soleymanlou et al., 2005; Ferreira et al., 2020; Myatt, 2010). Together, these data highlight the relevance of trophoblast ferroptosis and macro-blebbing to placental ferroptotic damage and common obstetrical disease.

MATERIALS AND METHODS

Cell culture

The collection of placentas used for isolation and culture of PHT and PPF cells was reviewed and approved by the Institutional Review Board at the University of Pittsburgh. PHT cells were isolated from placentas of uncomplicated pregnancies, according to our previously published, exempt protocol (Mouillet et al., 2010). They were maintained in Dulbecco's modified Eagle's medium (DMEM; Sigma-Aldrich, St Louis, MI) containing 10% bovine growth serum (HyClone, Logan, UT) and 1% antibiotics at 37°C in a 5% CO_2 air atmosphere. Cell quality was monitored by microscopy and by examining production of human chorionic gonadotropin, quantified by enzyme immunoassay (EIA, DRG, Marburg, Germany). BeWo cells (ATCC, Rockville, MD) were maintained in F12K Kaighn's modified medium supplemented with 10% SuperCalf serum (GemCell, Sacramento, CA). PPF cells were isolated during the preparation of PHT cells as we previously detailed (Li et al., 2020) and were cultured in DMEM (Sigma) supplemented with 10% SuperCalf serum. Human MDA-MB-231, U2OS, Hela and Caco2 cells (all from ATCC) were cultured in DMEM supplemented with 10% SuperCalf serum. HUVECs (ATCC) were maintained in endothelial cell basal medium-2 (Lonza, San Diego, CA) supplemented with 5% fetal bovine serum. All cell lines are routine tested in our lab for mycoplasma, and monitored for infections. Some of the cultures were performed in the presence of RSL3 (Selleck Chemicals, Houston, TX), which was used at variable concentrations and times, adjusted to experimental goals. Other ligands included staurosporine (Cell Signaling, Danvers, MA), forskolin (Sigma) and blebbistatin (Sigma). Ferrostatin-1 (Selleck) was used to block ferroptosis or to inhibit spontaneous ferroptosis in *GPX4* KD BeWo cells.

Analysis of blebbing, conditioned medium transfer, and cell co-culture

Cultured cells were routinely examined using a Zeiss Axiovert 40 microscope (Zeiss, Jena, Germany) with a 20× objective, equipped with a

DS-Qi1 digital camera (Nikon, Melville, NY). To capture and count blebs, we seeded 1.5×10^5 cells in 12-well plates. Cells were exposed to RSL3 after reaching 70–80% confluency. All membrane protrusion and detached blebs, normalized to cell number, were counted, excluding small blebs that were less than 10% of the cell diameter.

For CM transfer experiments, *shGPX4* and shControl BeWo cells were washed with phosphate-buffered saline (PBS) and cultured in serum-free medium for 24 h. CM was harvested after confirming ferroptosis in *shGPX4* cells but not in shControl cells. After centrifugation at 500 ***g*** for 10 min, the CM was applied to recipient BeWo cells for 8 h. The CM was then replaced with serum-free medium that contained RSL3 (25 nM) to trigger ferroptosis. The exposure to CM was performed before cell density in the recipient cells reached 80%. After 24 h of RSL3, the medium from recipient cells was collected for the LDH assay.

For co-culture experiments, control BeWo cells expressing RFP or BeWo cells expressing *shGPX4*-GFP (see below for transfection method) were seeded in glass-bottom 35-mm Petri dishes (MatTek, Ashland, MA) at a density of 3×10^5 cells and grown in full cell medium for 24 h. For a control dish, RFP BeWo cells were co-cultured with WT BeWo cells expressing GFP. After washing with PBS, the cells were stained with DAPI (Invitrogen, Carlsbad, CA) at room temperature (RT) for 5 min. To induce ferroptosis, the cells were exposed to RSL3 (100 nM). The images were taken after confirming blebbing in *shGPX4* cells in the separate culture and were captured by a Nikon A1 confocal microscope. Similarly, *PLA2G6*-KO BeWo cells expressing RFP were co-cultured with WT BeWo cells expressing GFP. For the control, BeWo cells expressing GFP were co-cultured with cells expressing RFP. Blebbing was analyzed using microscopy, as above.

Live-cell staining

For cell labeling, cultured BeWo or PHT cells were seeded in glass-bottom 35-mm Petri dishes (MatTek) at a density of 3×10^5 cells and grown in DMEM plus bovine growth medium for 24 h. After washing, the cells were stained with DAPI (Invitrogen) at RT for 5 min. The cells were then incubated with each dye, including CellMask, MitoTracker, LysoTracker and Bodipy 493/503, and diluted to a final concentration as listed in Table S2. After incubation, the staining solution was replaced with fresh serum-free medium. For F-actin, we used F-actin mRNA LifeAct-TagGFP2 (ibidi, Fitchburg, WI) according to the manufacturer's instructions. Cells were seeded at 3×10^5 in a glass-bottom 35-mm Petri dish (MatTek). The mRNA was incubated with 2 µl neutralization buffer (Fuse-It-mRNA easy, ibidi) for 10 min at RT, and the fusogenic solution was added to the cells for 20 min at 37°C and then replaced with fresh culture medium. The images were taken 24 h after transfection. For induction of ferroptosis, cells were exposed to 400-600 nM of RSL3 until all the cells showed signs of ferroptosis before imaging. Each probe-stained cell type was imaged by our Nikon A1 confocal microscope.

Isolation of extracellular vesicles

EVs were isolated as previously described (Ouyang et al., 2016). Briefly, the CM was collected as mentioned above and centrifuged at 500 ***g*** for 10 min. The supernatant was further centrifuged at 2500 ***g*** for 20 min to isolate ABs, which were washed and resuspended in PBS. For MV isolation, the supernatant was centrifuged at 12,000 ***g*** for 30 min, washed and resuspended in PBS. For isolation of sEVs, the supernatant was centrifuged at 100,000 ***g*** for 1 h, washed, and centrifuged at 100,000 ***g*** for 4 h, then resuspended in PBS. EV protein concentration was determined using Micro BCA according to the manufacturer's (Thermo Fisher Scientific, Waltham, MA) directions, and the quality was verified as described (Ouyang et al., 2016), using western immunoblotting and nanoparticle tracking analysis (NanoSight, Malvern Panalytical, Westborough, MA). After washing, the cells were cultured in serum-free medium and exposed to EVs (120 µg/well) for 24 h, followed by LDH release assay.

LDH analysis for cell viability

Measurement of LDH release was performed by using CytoTox-ONE (Promega, Madison, WI), following the manufacturer's instructions. After the cells were exposed to RSL3, the supernatant (100 µl) was transferred into a 96-well multiwell plate (Thermo Fisher). To extract total LDH, the cells were processed with 0.2% Triton-X (Sigma) for 10 min; 100 µl of the assay buffer were added to each well, and the plates were incubated for 10 min. Fluorescence was measured at 560 nm excitation and 590 nm emission, using a microplate reader (Molecular Devices, San Jose, CA). Cell viability (%) was calculated by dividing released LDH in the medium (after subtracting medium background) by total cellular LDH and presented as percent released LDH.

Cell transfection, silencing and KO cells

BeWo cells knocked out for *PLA2G6* have been previously described (Beharier et al., 2020). The shRNA silencing sequences (Table S1) for syncytin-1 (TRCN0000412806) and -2 (TRCN0000062256) were synthesized by Sigma-Aldrich. The sequence for *shGPX4* was as we previously detailed (Beharier et al., 2020). Briefly, the HEK293T packaging cell line (ATCC) was transfected with shRNA with PMD2.G (Addgene #12259, Watertown, MA) and psPAX2 (Addgene #12260) plasmids, using TransIT-Lenti transfection reagent (Mirus, Madison, WI). Lentiviral particles were harvested after 48 h. BeWo cells, cultured in 6-well plates to 50–60% confluence, were infected with lentiviral particles with Polybrene (5 µg/ml, Santa Cruz Biotechnology, Santa Cruz, CA). After 24 h, the virus-containing medium was replaced with fresh medium. After an additional 24 h, the cells were transferred to a new dish, followed by antibiotic-based selection using puromycin (2 µg/ml, InvivoGen, San Diego, CA). For co-culture experiments, BeWo cells were transfected with either pcDNA3-EGFP (Addgene #13031) or pcDNA3-RFP (Addgene #13032), using Lipofectamine 3000 (Thermo Fisher), following the manufacturer's protocol. After 48 h of transfection, stable clones were selected with 0.5 mg/ml G418 (Thermo Fisher). For analysis of endoplasmic reticulum, BeWo cells were transfected with the pcDNA3pENTR1A plasmid, which expresses the mNeonGreen tagged at the C-terminus to the endoplasmic reticulum retention signal KDEL (a gift from Mads Breun Larsen, Universisty of Pittsburgh, USA), with stable transfectants selected 0.5 mg/ml G418 (Gibco).

Reverse transcriptase and quantitative PCR

RNA was extracted from cells with TRI Reagent (Sigma). cDNA was synthesized from 1 µg of total RNA by using the High-Capacity cDNA Reverse Transcription kit (Applied Biosystems, Foster City, CA) according to the manufacturer's protocol. Template cDNA was PCR-amplified with the gene-specific primer sets (Table S1). RT-qPCR was performed using SYBR Select (Applied Biosystems) in a ViiA 7 system (Applied Biosystems). Analysis of qPCR data was performed using the ΔΔCt method (Livak and Schmittgen, 2001), normalized to glyceraldehyde-3-phosphate dehydrogenase expression.

Western blotting

The cells were lysed in a lysis buffer containing 150 mM NaCl, 20 mM HEPES (Thermo Fisher) pH 7.4, and 0.5% Triton X-100 (Sigma), supplemented with protease inhibitors and phosphatase inhibitor cocktail tablets (Thermo Fisher). Proteins were separated on SDS-PAGE and transferred to polyvinylidene fluoride membranes (Bio-Rad, Hercules, CA) as we previously described (Li et al., 2020). Membranes were blocked in 5% nonfat milk with 50 mM Tris-buffered saline (TBS) and 0.1% Tween 20 (Bio-Rad) and incubated overnight at 4°C with various primary antibodies (Table S2). After washing in TBS with Tween 20, each membrane was incubated with the appropriate horseradish peroxidase secondary antibody for 1 h at RT. Signals were detected using a ChemiDoc MP imaging system (Bio-Rad).

iPGell

BeWo cells were cultured in 10-cm culture dishes with 80–90% confluency. After exposure to RSL3, the medium was removed carefully to avoid damaging to the blebs. The cells and blebs were collected gently with a cell scraper. and 50 µl were mixed with 10 µl of A-solution of iPGell (GenoStaff, Tokyo, Japan), followed by B-solution. The structures were fixed in 4% paraformaldehyde (PFA, Electron Microscopy Science, Hatfield, PA) after the mixture had solidified (1–2 min) and processed for paraffin embedding.

Immunofluorescence

For immunofluorescence analysis of blebs and macro-vesicles, cells were collected and gelled with iPGell as described above. Sections (5 µm) of PFA-fixed, paraffin-embedded slides were used for antigen retrieval in citrate buffer (Santa Cruz Biotechnology, Dallas, TX) for 10 min at 95°C. After PBS washes, the cells were pre-incubated with 5% normal goat serum or 2% bovine serum albumin (Thermo Fisher) in PBS for 30 min at RT, followed by incubation with anti-α-tubulin primary antibody, as listed in Table S2, overnight at 4°C. After washing, the cells were incubated with fluorescently coupled anti-mouse-IgG antibody in blocking buffer for 60 min at RT. The nuclei were stained with DAPI (Thermo Fisher). All images were captured using a Nikon A1 confocal microscope.

Molecular simulations of unhydroperoxidized SAPE and SAPC lipid bilayers

Molecular dynamics simulations were carried out for SAPE and SAPC lipid bilayers, using the coarse-grained MARTINI force-field, version 2.2, implemented in the GROMACS version 2018.2 software (Abraham et al., 2015; Páll et al., 2015; Pronk et al., 2013). In the MARTINI model, about four heavy atoms and associated hydrogens are grouped into one particle, with the 16 (20) carbon atoms along the saturated (or unsaturated) fatty acid tail mapping to five particles. PC lipids had NC_3 in their head-group, whereas PE lipids had NH_3, with the latter being able to form hydrogen bonds with neighboring PE head-groups. This is reflected by the lower van der Waals potential energy minimum at the equilibrium distance between two NH_3 particles compared to that between two NC_3 particles in the MARTINI force-field.

The initial configurations and simulation set-up files for the lipid bilayers were generated using the Martini Bilayer Maker (Qi et al., 2015) within the CHARMM-GUI Web-based platform (Jo et al., 2008). Planar bilayers were generated with 1024 lipids per monolayer, and 4-nm-thick water layers above and below the bilayer. After energy minimization steps, molecular dynamics simulations were carried out with progressively reduced restraints on lipid head-group positions as the simulation time-step increased from 2 to 20 fs. Unrestrained simulations were then carried out for 2 µs to obtain the equilibrated configuration. Electrostatic interactions were computed using the reaction field method with a dielectric constant of 15 and cut-off distance of 1.1 nm. Van der Waals interactions were computed using the cut-off method, with the same distance of 1.1 nm. System temperature was maintained at 310 K with a velocity-rescaling thermostat; pressure was maintained at 1 bar (100 kPa) with a Parrinello-Rahman barostat with semi-isotropic coupling (*X-Y* plane coupled separately from the *Z* or bilayer normal direction) and a time-constant of 12 ps and compressibility of 3×10^{-4} bar^{-1}.

Molecular simulations of hydroperoxidized SAPE and SAPC lipid bilayers

From the equilibrated configurations of SAPE or SAPC bilayers, we constructed lipid bilayers with varying fractions of hydroperoxidized lipids by attaching OOH particles to either the particle representing carbon-12 (C12) or that representing carbon-15 (C15) on the unsaturated fatty acid tails. This procedure was performed using an in-house Python script (available upon request), which added a P2-type particle at 0.33 nm from the C12 or C15 particle along a vector that was the summation of bond vectors on two sides of the C12 or C15 particle on the fatty acid tail, following Thalmann's protocol (Guo et al., 2016). For example, the vectors along the D3A-to-D4A bond and C5A-to-D4A bond were added to produce the direction of the D4A-OOH bond (see Fig. 1A for the SAPE CG model). A similar procedure was done for the C12 attachment, where a D3A particle was used. No bending potential was added between the D3A-OOH or D4A-OOH bond and the rest of the lipid chain. Molecular dynamics simulations were then carried out for the bilayers, following the same procedure as for unhydroperoxidized bilayers detailed above.

Characterization of the physical and mechanical properties of bilayers

Physical and mechanical properties of the SAPE and SAPC bilayers were extracted from the 1- to 2-µs simulation trajectories. The area/lipid was taken as the lateral simulation box area divided by the number of lipids in each monolayer. The bilayer thickness was obtained from the separation of the means of the respective frequency distributions of PO_4 particle locations (marking the bilayer–water interface) in each monolayer, averaged over simulation trajectories. The level of disorder of the lipids in the bilayers was quantified by calculating the order parameter $P_2=(1/2)(3\cos^2\langle\theta\rangle-1)$, where $\langle\theta\rangle$ is an average of the angle between a selected lipid bond and the bilayer normal over all the lipids in the system and over the last 1 µs of simulation. By definition, P_2 has a maximum value of 1 and minimum value of −0.5. The order parameter was calculated using an in-house TCL script running on the Visual Molecular Dynamics software (Humphrey et al., 1996). The elastic modulus K_A of the lipid bilayers was calculated via a procedure whereby constant forces were applied by specifying a negative value for pressure, P_{Lat}, in the *X-Y* plane of the bilayer following (Leontiadou et al., 2004) to stretch it to a constant tension level. The membrane tension was then calculated from the external pressure applied to the system as $\sigma=L_z(P_z-P_{Lat})$ (Leontiadou et al., 2004), where L_z is the size of the simulation box in the Z-direction, and P_z is the pressure along the Z-direction (maintained at 1 bar). P_{Lat} values ranging from −5 bar to −30 bar were used. The membrane tension values were then plotted against the fractional change in membrane area, and K_A was taken as the slope of the linear regression fit to the curve within low tension regions. Selected membrane tension versus fractional change in strain area curves are shown in Fig. S4A,B for SAPE and SAPC bilayers, respectively.

Statistical analysis

Each experiment was performed at least three times, as detailed in the figure legends and based on past experience. Unpaired *t*-tests were used to compare means of samples from two independent groups. One-way analysis of variance (ANOVA) was used to compare the means of each sample with more than two independent groups, followed by Tukey's post hoc test. The data are presented as the mean±s.d. of the mean. $P<0.05$ was considered significant.

Acknowledgements

We thank Elena Sadovsky and Tiffany Coon for technical assistance, Lori Rideout for assistance with manuscript preparation, and Bruce Campbell for editing. We are grateful to Dr Mads Breun Larsen (University of Pittsburgh) for the mNeonGreen-KDEL plasmid. The computational work for this article was fully performed on resources of the National Supercomputing Centre, Singapore (https://www.nscc.sg).

Competing interests

Y.S. is a consultant at Illumina, Inc. The other authors report no conflicts.

Author contributions

Conceptualization: K.K., O.B., C.H., V.E.K., K.J.H., Y.S.; Methodology: K.K., O.B., C.H., V.E.K., K.J.H., Y.S.; Formal analysis: K.K., O.B., C.-P.C., C.H., K.J.H., Y.S.; Investigation: K.K., O.B., C.-P.C., J.P.G., Y.O., C.M.S.C.; Writing - original draft: K.K., O.B., C.-P.C., C.H., V.E.K., K.J.H., Y.S.; Writing - review & editing: O.B., V.E.K., K.J.H., Y.S.; Visualization: K.J.H., Y.S.; Supervision: K.J.H., Y.S.; Project administration: Y.S.; Funding acquisition: K.K., O.B., V.E.K., C.H., K.J.H., Y.S.

Funding

The project was supported by the following National Institutes of Health (NIH) grants: P01 HD069316 (to Y.S.), R01 HD086325 (to Y.S., K.J.H., C.H.), U01 AI156924, R01 AI145406, P01 HL114453, R01 CA165065 (to V.E.K.), the 25 Club of Magee-Womens Hospital (to Y.S.), a Magee-Womens Research Institute Postdoctoral Fellowship (to O.B.), the Jikei University School of Medicine Department of Obstetrics and Gynecology (to K.K.), Nanyang Technological University start-up grants M4082428.050 (to K.J.H.) and M4082352.050 (to C.H.), and Ministry of Education - Singapore, Academic Research Fund Tier 1 Award M4012229.050 (to C.H.). Deposited in PMC for release after 12 months.

Peer review history

The peer review history is available online at https://journals.biologists.com/jcs/article-lookup/DOI/10.1242/jcs.255737

References

Abraham, M. J., Murtola, T., Schulz, R., Páll, S., Smith, J. C., Hess, B. and Lindahl, E. (2015). GROMACS: high performance molecular simulations through multi-level parallelism from laptops to supercomputers. *SoftwareX* **1-2**, 19-25. doi:10.1016/j.softx.2015.06.001

Agmon, E., Solon, J., Bassereau, P. and Stockwell, B. R. (2018). Modeling the effects of lipid peroxidation during ferroptosis on membrane properties. *Sci. Rep.* **8**, 5155. doi:10.1038/s41598-018-23408-0

Alotaibi, M., Arrowsmith, S. and Wray, S. (2015). Hypoxia-induced force increase (HIFI) is a novel mechanism underlying the strengthening of labor contractions, produced by hypoxic stresses. *Proc. Natl. Acad. Sci. USA* **112**, 9763-9768. doi:10.1073/pnas.1503497112

Anthonymuthu, T. S., Kenny, E. M., Shrivastava, I., Tyurina, Y. Y., Hier, Z. E., Ting, H.-C., Dar, H. H., Tyurin, V. A., Nesterova, A., Amoscato, A. A. et al. (2018). Empowerment of 15-Lipoxygenase catalytic competence in selective oxidation of membrane ETE-PE to ferroptotic death signals, HpETE-PE. *J. Am. Chem. Soc.* **140**, 17835-17839. doi:10.1021/jacs.8b09913

Aoki, K., Satoi, S., Harada, S., Uchida, S., Iwasa, Y. and Ikenouchi, J. (2020). Coordinated changes in cell membrane and cytoplasm during maturation of apoptotic bleb. *Mol. Biol. Cell* **31**, 833-844. doi:10.1091/mbc.E19-12-0691

Beharier, O., Tyurin, V. A., Goff, J. P., Guerrero-Santoro, J., Kajiwara, K., Chu, T., Tyurina, Y. Y., St Croix, C. M., Wallace, C. T., Parry, S. et al. (2020). PLA2G6 guards placental trophoblasts against ferroptotic injury. *Proc. Natl. Acad. Sci. USA* **117**, 27319-27328. doi:10.1073/pnas.2009201117

Belavgeni, A., Bornstein, S. R., Von Mässenhausen, A., Tonnus, W., Stumpf, J., Meyer, C., Othmar, E., Latk, M., Kanczkowski, W., Kroiss, M. et al. (2019). Exquisite sensitivity of adrenocortical carcinomas to induction of ferroptosis. *Proc. Natl. Acad. Sci. USA* **116**, 22269-22274. doi:10.1073/pnas.1912700116

Brar, H. S., Platt, L. D., Devore, G. R., Horenstein, J. and Medearis, A. L. (1988). Qualitative assessment of maternal uterine and fetal umbilical artery blood flow and resistance in laboring patients by Doppler velocimetry. *Am. J. Obstet. Gynecol.* **158**, 952-956. doi:10.1016/0002-9378(88)90100-7

Brown, C. W., Amante, J. J., Chhoy, P., Elaimy, A. L., Liu, H., Zhu, L. J., Baer, C. E., Dixon, S. J. and Mercurio, A. M. (2019). Prominin2 drives ferroptosis resistance by stimulating iron export. *Dev. Cell* **51**, 575-586.e574. doi:10.1016/j.devcel.2019.10.007

Burton, G. J. and Jauniaux, E. (2018). Pathophysiology of placental-derived fetal growth restriction. *Am. J. Obstet. Gynecol.* **218**, S745-s761. doi:10.1016/j.ajog.2017.11.577

Burton, G. J., Watson, A. L., Hempstock, J., Skepper, J. N. and Jauniaux, E. (2002). Uterine glands provide histiotrophic nutrition for the human fetus during the first trimester of pregnancy. *J. Clin. Endocrinol. Metab.* **87**, 2954-2959. doi:10.1210/jcem.87.6.8563

Charras, G. and Paluch, E. (2008). Blebs lead the way: How to migrate without lamellipodia. *Nat. Rev. Mol. Cell Biol.* **9**, 730-736. doi:10.1038/nrm2453

Charras, G. T., Hu, C.-K., Coughlin, M. and Mitchison, T. J. (2006). Reassembly of contractile actin cortex in cell blebs. *J. Cell Biol.* **175**, 477-490. doi:10.1083/jcb.200602085

Claassen, D. A., Desler, M. M. and Rizzino, A. (2009). ROCK inhibition enhances the recovery and growth of cryopreserved human embryonic stem cells and human induced pluripotent stem cells. *Mol. Reprod. Dev.* **76**, 722-732. doi:10.1002/mrd.21021

Coleman, M. L., Sahai, E. A., Yeo, M., Bosch, M., Dewar, A. and Olson, M. F. (2001). Membrane blebbing during apoptosis results from caspase-mediated activation of ROCK I. *Nat. Cell Biol.* **3**, 339-345. doi:10.1038/35070009

Cunningham, C. C. (1995). Actin polymerization and intracellular solvent flow in cell surface blebbing. *J. Cell Biol.* **129**, 1589-1599. doi:10.1083/jcb.129.6.1589

Dai, E., Han, L., Liu, J., Xie, Y., Kroemer, G., Klionsky, D. J., Zeh, H. J., Kang, R., Wang, J. and Tang, D. (2020). Autophagy-dependent ferroptosis drives tumor-associated macrophage polarization via release and uptake of oncogenic KRAS protein. *Autophagy*, **16**, 2069-2083. doi:10.1080/15548627.2020.1714209

Dixon, S. J., Lemberg, K. M., Lamprecht, M. R., Skouta, R., Zaitsev, E. M., Gleason, C. E., Patel, D. N., Bauer, A. J., Cantley, A. M., Yang, W. S. et al. (2012). Ferroptosis: an iron-dependent form of nonapoptotic cell death. *Cell* **149**, 1060-1072. doi:10.1016/j.cell.2012.03.042

Doll, S. and Conrad, M. (2017). Iron and ferroptosis: a still ill-defined liaison. *IUBMB Life* **69**, 423-434. doi:10.1002/iub.1616

Doll, S., Freitas, F. P., Shah, R., Aldrovandi, M., Da Silva, M. C., Ingold, I., Goya Grocin, A., Xavier Da Silva, T. N., Panzilius, E., Scheel, C. H. et al. (2019). FSP1 is a glutathione-independent ferroptosis suppressor. *Nature,* **575**, 693-698. doi:10.1038/s41586-019-1707-0

Eleftheriadis, T., Pissas, G., Antoniadi, G., Liakopoulos, V. and Stefanidis, I. (2018). Cell death patterns due to warm ischemia or reperfusion in renal tubular epithelial cells originating from human, mouse, or the native hibernator hamster. *Biology (Basel)* **7**, 48. doi:10.3390/biology7040048

Fedier, A. and Keller, H. U. (1997). Suppression of bleb formation, locomotion, and polarity of Walker carcinosarcoma cells by hypertonic media correlates with cell volume reduction but not with changes in the F-actin content. *Cell Motil. Cytoskelet.* **37**, 326-337. doi:10.1002/(SICI)1097-0169(1997)37:4<326::AID-CM4>3.0.CO;2-2

Ferreira, R. C., Fragoso, M. B. T., Bueno, N. B., Goulart, M. O. F. and De Oliveira, A. C. M. (2020). Oxidative stress markers in preeclamptic placentas: A systematic review with meta-analysis. *Placenta* **99**, 89-100. doi:10.1016/j.placenta.2020.07.023

Fisher, A. L. and Nemeth, E. (2017). Iron homeostasis during pregnancy. *Am. J. Clin. Nutr.* **106**, 1567s-1574s. doi:10.3945/ajcn.117.155812

Friedmann Angeli, J. P., Schneider, M., Proneth, B., Tyurina, Y. Y., Tyurin, V. A., Hammond, V. J., Herbach, N., Aichler, M., Walch, A., Eggenhofer, E. et al. (2014). Inactivation of the ferroptosis regulator Gpx4 triggers acute renal failure in mice. *Nat. Cell Biol.* **16**, 1180-1191. doi:10.1038/ncb3064

Fuchs, Y. and Steller, H. (2011). Programmed cell death in animal development and disease. *Cell* **147**, 742-758. doi:10.1016/j.cell.2011.10.033

Galluzzi, L., Vitale, I., Aaronson, S. A., Abrams, J. M., Adam, D., Agostinis, P., Alnemri, E. S., Altucci, L., Amelio, I., Andrews, D. W., et al. (2018). Molecular mechanisms of cell death: recommendations of the nomenclature committee on Cell Death 2018. *Cell Death Differ.* **25**, 486-541. doi:10.1038/s41418-017-0012-4

Gao, M., Monian, P., Quadri, N., Ramasamy, R. and Jiang, X. (2015). Glutaminolysis and transferrin regulate ferroptosis. *Mol. Cell* **59**, 298-308. doi:10.1016/j.molcel.2015.06.011

Gerbaud, P. and Pidoux, G. (2015). Review: An overview of molecular events occurring in human trophoblast fusion. *Placenta* **36** Suppl. 1, S35-S42. doi:10.1016/j.placenta.2014.12.015

Gruenberg, J. and Van Der Goot, F. G. (2006). Mechanisms of pathogen entry through the endosomal compartments. *Nat. Rev. Mol. Cell Biol.* **7**, 495-504. doi:10.1038/nrm1959

Guo, Y., Baulin, V. A. and Thalmann, F. (2016). Peroxidised phospholipid bilayers: insight from coarse-grained molecular dynamics simulations. *Soft Matter* **12**, 263-271. doi:10.1039/C5SM01350J

Hernández, J. M. and Podbilewicz, B. (2017). The hallmarks of cell-cell fusion. *Development* **144**, 4481-4495. doi:10.1242/dev.155523

Hou, W., Xie, Y., Song, X., Sun, X., Lotze, M. T., Zeh, H. J., III, Kang, R. and Tang, D. (2016). Autophagy promotes ferroptosis by degradation of ferritin. *Autophagy* **12**, 1425-1428. doi:10.1080/15548627.2016.1187366

Humphrey, W., Dalke, A. and Schulten, K. (1996). VMD: visual molecular dynamics. *J Mol Graph* **14**, 33-38. doi:10.1016/0263-7855(96)00018-5

Hung, T.-H., Skepper, J. N., Charnock-Jones, D. S. and Burton, G. J. (2002). Hypoxia-reoxygenation: a potent inducer of apoptotic changes in the human placenta and possible etiological factor in preeclampsia. *Circ. Res.* **90**, 1274-1281. doi:10.1161/01.RES.0000024411.22110.AA

Jacobson, M. D., Weil, M. and Raff, M. C. (1997). Programmed cell death in animal development. *Cell* **88**, 347-354. doi:10.1016/S0092-8674(00)81873-5

Jansen, C., Tobita, C., Umemoto, E. U., Starkus, J., Rysavy, N. M., Shimoda, L. M. N., Sung, C., Stokes, A. J. and Turner, H. (2019). Calcium-dependent, non-apoptotic, large plasma membrane bleb formation in physiologically stimulated mast cells and basophils. *J. Extracell. Vesicles* **8**, 1578589. doi:10.1080/20013078.2019.1578589

Jo, S., Kim, T., Iyer, V. G. and Im, W. (2008). CHARMM-GUI: a web-based graphical user interface for CHARMM. *J. Comput. Chem.* **29**, 1859-1865. doi:10.1002/jcc.20945

Kagan, V. E., Mao, G., Qu, F., Angeli, J. P. F., Doll, S., Croix, C. S., Dar, H. H., Liu, B., Tyurin, V. A., Ritov, V. B. et al. (2017). Oxidized arachidonic and adrenic PEs navigate cells to ferroptosis. *Nat. Chem. Biol.* **13**, 81-90. doi:10.1038/nchembio.2238

Ke, Y., Fan, X., Rui, H., Xinjun, R., Dejia, W., Chuanzhen, Z. and Li, X. (2020). Exosomes derived from RPE cells under oxidative stress mediate inflammation and apoptosis of normal RPE cells through Apaf1/caspase-9 axis. *J. Cell. Biochem.* **121**, 4849-4861. doi:10.1002/jcb.29713

Kinowaki, Y., Kurata, M., Ishibashi, S., Ikeda, M., Tatsuzawa, A., Yamamoto, M., Miura, O., Kitagawa, M. and Yamamoto, K. (2018). Glutathione peroxidase 4 overexpression inhibits ROS-induced cell death in diffuse large B-cell lymphoma. *Lab. Invest.* **98**, 609-619. doi:10.1038/s41374-017-0008-1

Kwon, M.-Y., Park, E., Lee, S.-J. and Chung, S. W. (2015). Heme oxygenase-1 accelerates erastin-induced ferroptotic cell death. *Oncotarget* **6**, 24393-24403. doi:10.18632/oncotarget.5162

Lavialle, C., Cornelis, G., Dupressoir, A., Esnault, C., Heidmann, O., Vernochet, C. and Heidmann, T. (2013). Paleovirology of 'syncytins', retroviral env genes exapted for a role in placentation. *Philos. Trans. R. Soc. Lond. B Biol. Sci.* **368**, 20120507. doi:10.1098/rstb.2012.0507

Leontiadou, H., Mark, A. E. and Marrink, S. J. (2004). Molecular dynamics simulations of hydrophilic pores in lipid bilayers. *Biophys. J.* **86**, 2156-2164. doi:10.1016/S0006-3495(04)74275-7

Li, Q., Han, X., Lan, X., Gao, Y., Wan, J., Durham, F., Cheng, T., Yang, J., Wang, Z., Jiang, C. et al. (2017). Inhibition of neuronal ferroptosis protects hemorrhagic brain. *JCI Insight* **2**, e90777. doi:10.1172/jci.insight.90777

Li, H., Pinilla-Macua, I., Ouyang, Y., Sadovsky, E., Kajiwara, K., Sorkin, A. and Sadovsky, Y. (2020). Internalization of trophoblastic small extracellular vesicles and detection of their miRNA cargo in P-bodies. *J. Extracell Vesicles* **9**, 1812261. doi:10.1080/20013078.2020.1812261

Linkermann, A., Skouta, R., Himmerkus, N., Mulay, S. R., Dewitz, C., De Zen, F., Prokai, A., Zuchtriegel, G., Krombach, F., Welz, P.-S. et al. (2014a). Synchronized renal tubular cell death involves ferroptosis. *Proc. Natl. Acad. Sci. USA* **111**, 16836-16841. doi:10.1073/pnas.1415518111

Linkermann, A., Stockwell, B. R., Krautwald, S. and Anders, H. J. (2014b). Regulated cell death and inflammation: an auto-amplification loop causes organ failure. *Nat. Rev. Immunol.* **14**, 759-767. doi:10.1038/nri3743

Livak, K. J. and Schmittgen, T. D. (2001). Analysis of relative gene expression data using real-time quantitative PCR and the $2^{-\Delta\Delta CT}$ Method. *Methods* **25**, 402-408. doi:10.1006/meth.2001.1262

Ma, S., Dielschneider, R. F., Henson, E. S., Xiao, W., Choquette, T. R., Blankstein, A. R., Chen, Y. and Gibson, S. B. (2017). Ferroptosis and autophagy induced cell death occur independently after siramesine and lapatinib treatment in breast cancer cells. *PLoS ONE* **12**, e0182921. doi:10.1371/journal.pone.0182921

Maeda, T., Toyoda, F., Imai, S., Tanigawa, H., Kumagai, K., Matsuura, H. and Matsusue, Y. (2016). Lidocaine induces ROCK-dependent membrane blebbing and subsequent cell death in rabbit articular chondrocytes. *J. Orthop. Res.* **34**, 754-762. doi:10.1002/jor.23092

Mao, G., Li, T., Zou, Z., Qu, S. and Shi, M. (2014). Prestretch effect on snap-through instability of short-length tubular elastomeric balloons under inflation. *Int. J. Solids Structures* **51**, 2109-2115. doi:10.1016/j.ijsolstr.2014.02.013

Mercer, J. and Helenius, A. (2008). Vaccinia virus uses macropinocytosis and apoptotic mimicry to enter host cells. *Science,* **320**, 531-535. doi:10.1126/science.1155164

Mi, S., Lee, X., Li, X.-P., Veldman, G. M., Finnerty, H., Racie, L., Lavallie, E., Tang, X. Y., Edouard, P., Howes, S. et al. (2000). Syncytin is a captive retroviral envelope protein involved in human placental morphogenesis. *Nature* **403**, 785-789. doi:10.1038/35001608

Mistry, H. D., Kurlak, L. O., Williams, P. J., Ramsay, M. M., Symonds, M. E. and Broughton Pipkin, F. (2010). Differential expression and distribution of placental glutathione peroxidases 1, 3 and 4 in normal and preeclamptic pregnancy. *Placenta* **31**, 401-408. doi:10.1016/j.placenta.2010.02.011

Mouillet, J. F., Chu, T., Nelson, D. M., Mishima, T. and Sadovsky, Y. (2010). MiR-205 silences MED1 in hypoxic primary human trophoblasts. *FASEB J.* **24**, 2030-2039. doi:10.1096/fj.09-149724

Myatt, L. (2010). Review: Reactive oxygen and nitrogen species and functional adaptation of the placenta. *Placenta* **31** Suppl., S66-S69. doi:10.1016/j.placenta.2009.12.021

Nelson, D. M. (1996). Apoptotic changes occur in syncytiotrophoblast of human placental villi where fibrin type fibrinoid is deposited at discontinuities in the villous trophoblast. *Placenta* **17**, 387-391. doi:10.1016/S0143-4004(96)90019-3

Ng, S.-W., Norwitz, S. G. and Norwitz, E. R. (2019). The impact of iron overload and ferroptosis on reproductive disorders in humans: implications for preeclampsia. *Int. J. Mol. Sci.* **20**, 3283. doi:10.3390/ijms20133283

Nganga, R., Oleinik, N., Kim, J., Selvam, S. P., De Palma, R., Johnson, K. A., Parikh, R. Y., Gangaraju, V., Peterson, Y., Dany, M. et al. (2019). Receptor-interacting Ser/Thr kinase 1 (RIPK1) and myosin IIA-dependent ceramidosomes form membrane pores that mediate blebbing and necroptosis. *J. Biol. Chem.* **294**, 502-519. doi:10.1074/jbc.RA118.005865

Norman, L. L., Brugés, J., Sengupta, K., Sens, P. and Aranda-Espinoza, H. (2010). Cell blebbing and membrane area homeostasis in spreading and retracting cells. *Biophys. J.* **99**, 1726-1733. doi:10.1016/j.bpj.2010.07.031

Ouyang, Y., Bayer, A., Chu, T., Tyurin, V. A., Kagan, V. E., Morelli, A. E., Coyne, C. B. and Sadovsky, Y. (2016). Isolation of human trophoblastic extracellular vesicles and characterization of their cargo and antiviral activity. *Placenta* **47**, 86-95. doi:10.1016/j.placenta.2016.09.008

Páll, S., Abraham, M. J., Kutzner, C., Hess, B. and Lindahl, E. (2015). Tackling exascale software challenges in molecular dynamics simulations with GROMACS. In International Conference on Exascale Applications and Software 2014 (ed. S. Markidis and E. Laure), pp. 3-27. Stockholm, Sweden. Springer International Publishing.

Peng, X., Lin, Y., Li, J., Liu, M., Wang, J., Li, X., Liu, J., Jia, X., Jing, Z., Huang, Z. et al. (2016). Evaluation of Glutathione Peroxidase 4 role in preeclampsia. *Sci. Rep.* **6**, 33300. doi:10.1038/srep33300

Peng, C.-P., Sadovsky, Y., Hsia, K. J. and Huang, C. (2021). Site-specific peroxidation modulates lipid bilayer mechanics. *Extreme Mech. Lett.* **42**, 101148. doi:10.1016/j.eml.2020.101148.

Pronk, S., Páll, S., Schulz, R., Larsson, P., Bjelkmar, P., Apostolov, R., Shirts, M. R., Smith, J. C., Kasson, P. M., Van Der Spoel, D. et al. (2013). GROMACS 4.5: a high-throughput and highly parallel open source molecular simulation toolkit. *Bioinformatics* **29**, 845-854. doi:10.1093/bioinformatics/btt055

Qi, Y., Ingólfsson, H. I., Cheng, X., Lee, J., Marrink, S. J. and Im, W. (2015). CHARMM-GUI Martini Maker for coarse-grained simulations with the Martini force field. *J. Chem. Theory Comput.* **11**, 4486-4494. doi:10.1021/acs.jctc.5b00513

Rosa, R. D., Spinozzi, F. and Itri, R. (2018). Hydroperoxide and carboxyl groups preferential location in oxidized biomembranes experimentally determined by small angle X-ray scattering: implications in membrane structure. *Biochim. Biophys. Acta Biomembr.* **1860**, 2299-2307. doi:10.1016/j.bbamem.2018.05.011

Ruan, R., Zou, L., Sun, S., Liu, J., Wen, L., Gao, D. and Ding, W. (2015). Cell blebbing upon addition of cryoprotectants: a self-protection mechanism. *PLoS ONE* **10**, e0125746. doi:10.1371/journal.pone.0125746

Schoots, M. H., Gordijn, S. J., Scherjon, S. A., Van Goor, H. and Hillebrands, J.-L. (2018). Oxidative stress in placental pathology. *Placenta* **69**, 153-161. doi:10.1016/j.placenta.2018.03.003

Sebbagh, M., Renvoizé, C., Hamelin, J., Riché, N., Bertoglio, J. and Bréard, J. (2001). Caspase-3-mediated cleavage of ROCK I induces MLC phosphorylation and apoptotic membrane blebbing. *Nat. Cell Biol.* **3**, 346-352. doi:10.1038/35070019

Semenza, J. C., Hardwick, K. G., Dean, N. and Pelham, H. R. B. (1990). ERD2, a yeast gene required for the receptor-mediated retrieval of luminal ER proteins from the secretory pathway. *Cell* **61**, 1349-1357. doi:10.1016/0092-8674(90)90698-E

Shen, T., Huang, Z., Shi, C., Pu, X., Xu, X., Wu, Z., Ding, G. and Cao, L. (2020). Pancreatic cancer-derived exosomes induce apoptosis of T lymphocytes through the p38 MAPK-mediated endoplasmic reticulum stress. *FASEB J.* **34**, 8442-8458. doi:10.1096/fj.201902186R

Shi, X., Gillespie, P. G. and Nuttall, A. L. (2005). Na+ influx triggers bleb formation on inner hair cells. *Am. J. Physiol. Cell Physiol.* **288**, C1332-C1341. doi:10.1152/ajpcell.00522.2004

Soares, M. J., Iqbal, K. and Kozai, K. (2017). Hypoxia and placental development. *Birth Defects Res.* **109**, 1309-1329. doi:10.1002/bdr2.1135

Soleymanlou, N., Jurisica, I., Nevo, O., Ietta, F., Zhang, X., Zamudio, S., Post, M. and Caniggia, I. (2005). Molecular evidence of placental hypoxia in preeclampsia. *J. Clin. Endocrinol. Metab.* **90**, 4299-4308. doi:10.1210/jc.2005-0078

Sun, X., Ou, Z., Chen, R., Niu, X., Chen, D., Kang, R. and Tang, D. (2016). Activation of the p62-Keap1-NRF2 pathway protects against ferroptosis in hepatocellular carcinoma cells. *Hepatology* **63**, 173-184. doi:10.1002/hep.28251

Taneja, N., Bersi, M. R., Baillargeon, S. M., Fenix, A. M., Cooper, J. A., Ohi, R., Gama, V., Merryman, W. D. and Burnette, D. T. (2020). Precise tuning of cortical contractility regulates cell shape during cytokinesis. *Cell Rep.* **31**, 107477. doi:10.1016/j.celrep.2020.03.041

Tinevez, J.-Y., Schulze, U., Salbreux, G., Roensch, J., Joanny, J.-F. and Paluch, E. (2009). Role of cortical tension in bleb growth. *Proc. Natl. Acad. Sci. USA* **106**, 18581-18586. doi:10.1073/pnas.0903353106

Tuo, Q.-Z., Lei, P., Jackman, K. A., Li, X.-L., Xiong, H., Li, X.-L., Liuyang, Z.-Y., Roisman, L., Zhang, S.-T., Ayton, S. et al. (2017). Tau-mediated iron export prevents ferroptotic damage after ischemic stroke. *Mol. Psychiatry* **22**, 1520-1530. doi:10.1038/mp.2017.171

Voura, E. B., Sandig, M. and Siu, C.-H. (1998). Cell-cell interactions during transendothelial migration of tumor cells. *Microsc. Res. Tech.* **43**, 265-275. doi:10.1002/(SICI)1097-0029(19981101)43:3<265::AID-JEMT9>3.0.CO;2-Z

Wang, H., Liu, C., Zhao, Y. and Gao, G. (2020). Mitochondria regulation in ferroptosis. *Eur. J. Cell Biol.* **99**, 151058. doi:10.1016/j.ejcb.2019.151058

Weber, G., Charitat, T., Baptista, M. S., Uchoa, A. F., Pavani, C., Junqueira, H. C., Guo, Y., Baulin, V. A., Itri, R., Marques, C. M. et al. (2014). Lipid oxidation induces structural changes in biomimetic membranes. *Soft Matter* **10**, 4241-4247. doi:10.1039/c3sm52740a

Wenzel, S. E., Tyurina, Y. Y., Zhao, J., St. Croix, C. M., Dar, H. H., Mao, G., Tyurin, V. A., Anthonymuthu, T. S., Kapralov, A. A., Amoscato, A. A. et al. (2017). PEBP1 wardens ferroptosis by enabling lipoxygenase generation of lipid death signals. *Cell* **171**, 628-641.e626. doi:10.1016/j.cell.2017.09.044

Wu, J., Minikes, A. M., Gao, M., Bian, H., Li, Y., Stockwell, B. R., Chen, Z.-N. and Jiang, X. (2019). Intercellular interaction dictates cancer cell ferroptosis via NF2-YAP signalling. *Nature* **572**, 402-406. doi:10.1038/s41586-019-1426-6

Xie, Y., Hou, W., Song, X., Yu, Y., Huang, J., Sun, X., Kang, R. and Tang, D. (2016). Ferroptosis: process and function. *Cell Death Differ.* **23**, 369-379. doi:10.1038/cdd.2015.158

Yang, W.-H., Ding, C.-K. C., Sun, T., Rupprecht, G., Lin, C.-C., Hsu, D. and Chi, J.-T. (2019). The Hippo Pathway effector TAZ regulates ferroptosis in renal cell carcinoma. *Cell Rep.* **28**, 2501-2508.e4. doi:10.1016/j.celrep.2019.07.107

Yang, W. S., Sriramaratnam, R., Welsch, M. E., Shimada, K., Skouta, R., Viswanathan, V. S., Cheah, J. H., Clemons, P. A., Shamji, A. F., Clish, C. B. et al. (2014). Regulation of ferroptotic cancer cell death by GPX4. *Cell* **156**, 317-331. doi:10.1016/j.cell.2013.12.010

Zhang, H., He, Y., Wang, J.-X., Chen, M.-H., Xu, J.-J., Jiang, M.-H., Feng, Y.-L. and Gu, Y.-F. (2020). miR-30-5p-mediated ferroptosis of trophoblasts is implicated in the pathogenesis of preeclampsia. *Redox Biol.* **29**, 101402. doi:10.1016/j.redox.2019.101402

Zou, Y., Li, H., Graham, E. T., Deik, A. A., Eaton, J. K., Wang, W., Sandoval-Gomez, G., Clish, C. B., Doench, J. G. and Schreiber, S. L. (2020). Cytochrome P450 oxidoreductase contributes to phospholipid peroxidation in ferroptosis. *Nat. Chem. Biol.* **16**, 302-309. doi:10.1038/s41589-020-0472-6